Bulletin of the Seismological Society of America, Vol. 104, No. 3, pp. 1540–1549, June 2014, doi: 10.1785/0120130150

Short Note

Shear-Wave Birefringence Measurements in Faulted Near-Surface Sediment: Fluorspar Area Fault Complex, Central United States

by Edward W. Woolery and Ali Almayahi

Abstract The location and geometry of seismogenic faults are fundamental to understanding the regional seismic hazard; however, surface evidence for active faults in the seismically active central United States is rare, thus contributing to the uncertainty in the hazard estimation. Multicomponent *S*-wave reflection energy was acquired near the northern boundary of the New Madrid Seismic Zone across a well-constrained N61°E-oriented fault that extends above the top of Paleozoic bedrock and into near-surface Quaternary sediment in order to evaluate the effectiveness of shear-wave splitting measurements for determining azimuthal orientation of fault-deformed unlithified sediment that lack a surface manifestation. The data were analyzed within the shear-wave window (i.e., without wide-angle distortion) using orthogonal source–receiver orientations. Normalized reflection energy spectra of the main and cross-diagonal elements were rotated in 5° increments to determine fast (S1) and slow (S2) *S*-wave directions associated with the azimuthally anisotropic inclusion. The resultant natural coordinate system was N60°E and N30°W for S1 and S2, respectively. The S1 orientation correlated with the established N61°E fault strike. In addition, there was an average dynamic mistie of 11.3 ms that suggests 3.6% azimuthal anisotropy between the top of bedrock and ground surface. These results suggest that shear-wave birefringence can be a useful tool for defining azimuthal orientation of neotectonic inclusions that lack surface or geomorphic expression, as well as for areas that may have limited accessibility (i.e., urban environments) for deploying multiple widespread geophysical surveys.

Introduction

Shear-wave splitting is used in various applications and at a wide range of depth and scale. In the deep-earth interior, for example, it can be a tool for making inferences about the style and geometry of mantle flow because it is a direct consequence of deformation processes (Long and Silver, 2009); however, shear-wave birefringence was initially a successful tool for defining *in situ* stresses and fracture orientation in crustal rock formations (Crampin, 1985; Martin and Davis, 1987; Verdon and Kendall, 2011). Schoenberg and Sayers (1995) showed that the defined polarization related to the internal structure of rock (e.g., fracture orientation) can also provide second-order physical inference (e.g., preferred fluid flow directions). These representative examples are how the shear-wave splitting was traditionally applied in rock environments; it was Harris (1996), however, who first showed the surface shear-wave splitting technique may be effective for measuring sediment anisotropy in a seismic-hazard context. Specifically, Harris (1996) applied the shear-wave splitting method to sediment near the central part of the New Madrid Seismic Zone (NMSZ) and successfully identified azimuthal anisotropy that he attributed to differential stress conditions and/or associated microfractures.

Identifying and characterizing active faults in areas lacking surface expression is a challenging task, as exemplified in and near the NMSZ, including the Fluorspar area fault complex (FAFC) of western Kentucky (Fig. 1). Surface manifestations of active faults in this region are generally obscured by thick sequences of comparatively weak, water-saturated Mississippi embayment sediment that overlies bedrock. The soft sediment overburden and relatively long recurrence interval between large earthquakes conceal bedrock structure and commonly fail, apart from a few notable exceptions (e.g., Crowley's Ridge, Reelfoot Scarp, Commerce Geophysical lineament, and Sikeston Ridge), to produce significant or noticeable surficial tectonic-related geomorphology. In this study, we wanted to evaluate the *S*-wave birefringent response in fault-displaced sediment; however, many geologic processes or factors can induce

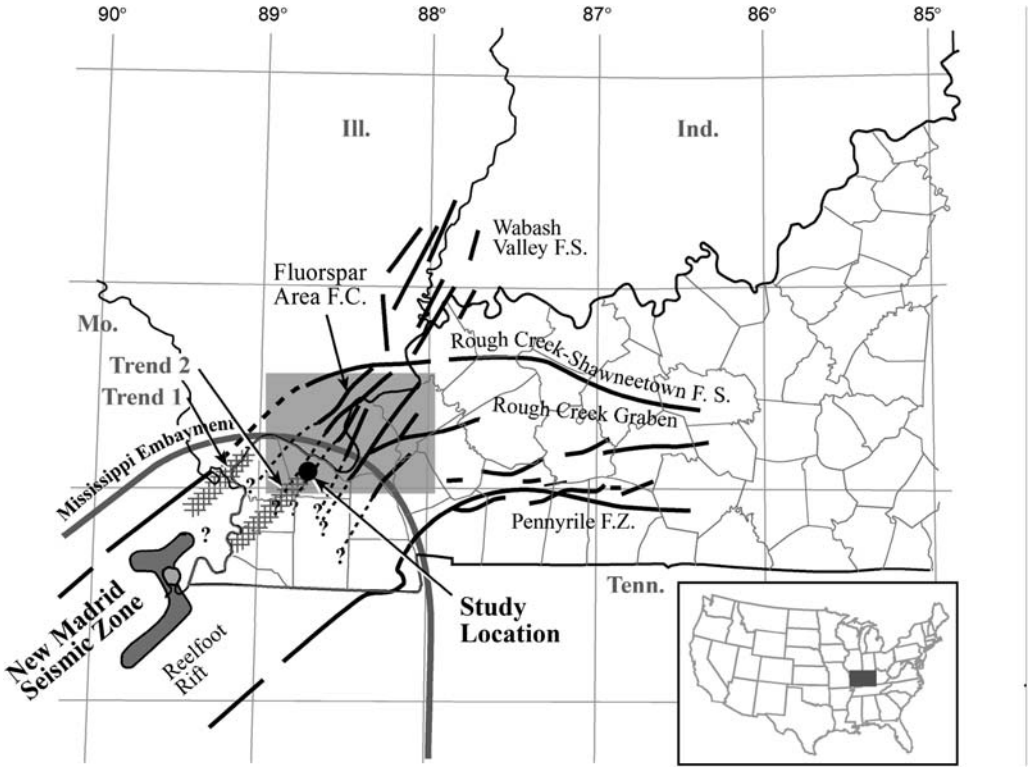

Figure 1. Major structural features in the central Mississippi Valley (the inset shows these structures' location in the central United States). The two linear northeast-oriented gray-hatched areas represent the locations of Wheeler (1997) trends 1 and 2 seismicity in relation to the primary New Madrid Seismic Zone (dark-gray shaded area) and the study site (black-filled circle). The light-gray shaded area is the location of the Fluorspar area fault complex (FAFC) shown in Figure 2 (modified from Kolata and Nelson, 1991; Woolery and Street, 2002).

azimuthal anisotropy (e.g., depositional fabric, mineralogy, differential stress, heat flow, fractures, faults, etc.). Consequently, in order to evaluate the fault influence on polarization in unlithified sediment and minimize effects from other potential factors, this study applied the technique specifically to a geometrically well-constrained fault that high-resolution seismic-reflection data shows to affect the entire resolvable sediment overburden.

Geologic Setting

The study area is located near the Ohio River in western Kentucky at the approximate juncture of two late Precambrian–early Paleozoic rifts, the Reelfoot Rift, and the Rough Creek graben (Kolata and Nelson, 1991) (Fig. 1). This area is also coincident with the northern end of the sediment-filled Mississippi embayment. The Rough Creek graben is bound on the north by the Rough Creek–Shawneetown fault system and extends from Kentucky into southern Illinois for about 25 km, then abruptly turns to the southwest and joins the Lusk Creek and Raum fault zones which form the northwestern boundary of the FAFC. The northwestern boundary of the fault complex is interpreted to continue southwest beneath the Late Cretaceous and younger sedimentary cover of the northern Mississippi embayment, where it forms the northwest margin of the Reelfoot Rift, the host geologic structure for the NMSZ (Kolata and Nelson, 1991).

Immediately north of the embayment, in southern Illinois, the FAFC outcrops, and was described by Nelson *et al.* (1997, 1999) as a series of strike-slip pull-apart grabens bounded by northeast-striking normal and inverted reverse faults (Figs. 1 and 2a). The primary fault strands (i.e., Lusk Creek, Raum, Hobbs Creek, and Barnes Creek) also show evidence of episodic dip-slip reactivation, as well as strike-slip movement that extend into the Quaternary section (Nelson *et al.*, 1999). To the south in western Kentucky, the Paleozoic bedrock is masked by several tens to a few hundred meters of the embayment sediment. Although there are no known surface fault expressions, prior near-surface seismic-reflection investigations in the area have shown the FAFC extends beneath the embayment cover with reactivated displacement extending into Quaternary (Pliestocene) sediments (Woolery and Street, 2002; Woolery *et al.*, 2009).

Stratigraphically, the Paleozoic limestone bedrock (Pz) at the site is unconformably overlain by approximately 100 m of unlithified sediments that are Late Cretaceous and younger (Olive, 1980) (Fig. 2b). The Paleocene Clayton and the upper Cretaceous McNairy Formations are undifferentiated due to their similarity and are classified together as the McNairy–Clayton Formation (K). The K is regionally overlain by the Paleocene-aged Porters Creek Clay; Sexton (2006), however, showed that the Porters Creek formation has been removed across the study site by the ancestral Tennessee River. Tertiary deposits overlie the Porters Creek.

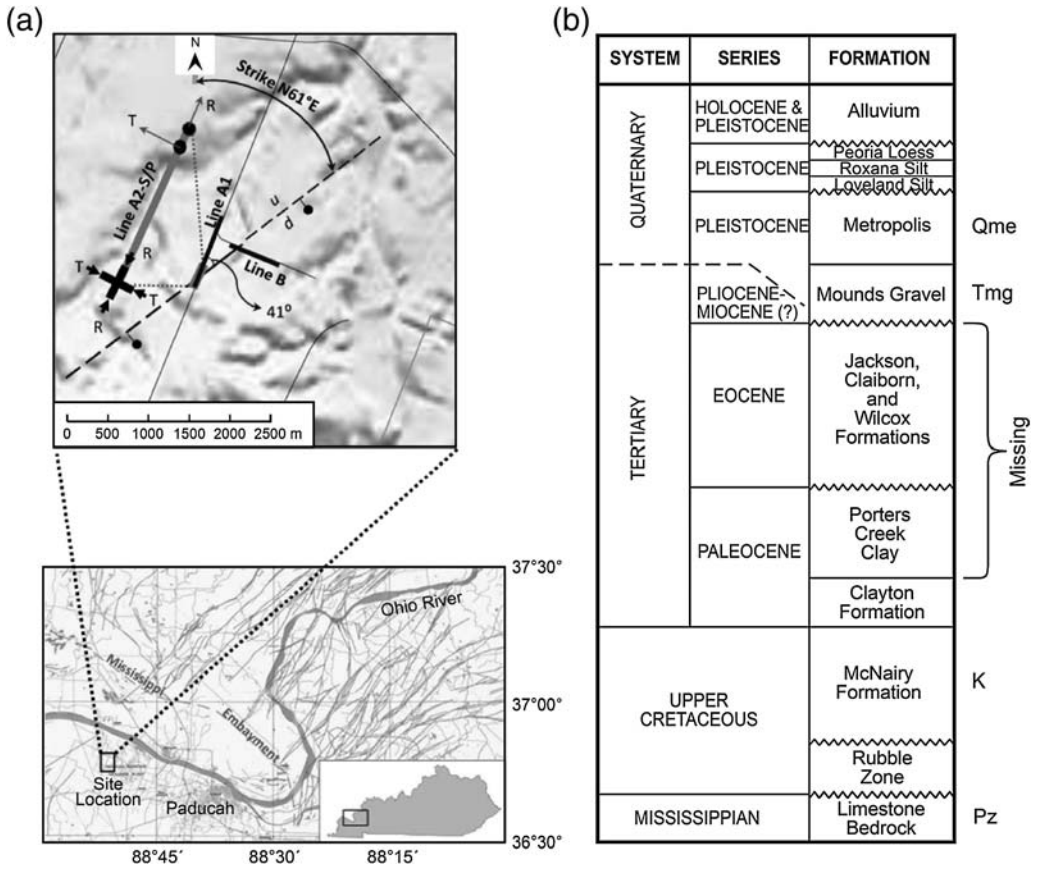

Figure 2. (a) The lower part of the figure shows the regional structural features projected on the Paducah and Murray 30 × 60 minute quadrangles. The FAFC projects beneath the Mississippi embayment sediment cover toward the study site. The enlarged inset shows our seismic surveys in relation to the interpreted well-constrained fault. Lines A1, A2-*P*, and A2-*S* were acquired coincident with one another. The bold-black cross at the southwestern end of line A2-*S* depict the transverse and radial source directions and the black-filled circles with gray arrows show the transverse and radial receiver configuration. Line B was a *P*-wave profile oriented orthogonal to the survey A lines. (b) Detailed site stratigraphy for approximately 100 m of post-Paleozoic unlithified sediment. The bedrock (Pz), undifferentiated Clayton–McNairy (K), Mounds gravel (Tmg), and metropolis (Qme) define the primary reflection events for the surveys (after Woolery and Street, 2002).

These sediments are early Eocene and are called the Wilcox formation. The Eocene sands and clays are separated from the Pleistocene loess by Pliocene–Pleistocene sands and gravels, locally referred to as the continental deposits. Nelson *et al.* (1997, 1999) differentiated the continental deposits into the Mounds gravel (Tmg) and the overlying metropolis formation (Qme). Glacial loess deposits overlie the continental deposits. Woolery and Street (2002) and Woolery *et al.* (2009) used a nearby borehole for seismostratigraphic correlation and also showed that the stratigraphic tops of the Pz, K, and Tmg are high-acoustic impedance boundaries and define the primary seismic-stratigraphy marker horizons for this area (Fig. 2b); the highest quality data can also resolve the loess–Qme boundary, however.

Target Fault: Data Acquisition, Processing, and Interpretation

The target fault for this experiment was selected based on high-resolution images and well-constrained orientation (Woolery and Street, 2002). From a total dataset that includes ~27 km of near-surface *SH*- and 6 km of *P*-wave reflection profiles, two adjacent and orthogonal profiles, called surveys A and B in this study, were selected because their clear definition of a correlative fault that exhibits a local N61°E strike (Fig. 2), as well as expressed deformation that extends above the Paleozoic bedrock to include the boundary separating the Quaternary metropolis formation and overlying loess. Having these geologic constraints were important because shear-wave splitting measurements using the seismic-reflection method are controlled by anisotropy near the receivers (Harris, 1996); therefore, a near-surface fault target that extends across most, if not all of the sediment overburden minimizes vertical variation and the effects of other frequency-dependent anisotropic factors such as those associated with weathering, erosion, and deposition phenomena.

The A and B surveys were collected along county highways and are composed of both *P*- and *SH*-wave data. Specifically, the N20°E-oriented survey A is composed of two *SH*-wave lines, A1 and A2-*S* (i.e., 30 Hz geophones and 2 m interval), and one *P*-wave line, A2-*P* (40 Hz geophones and 2 m interval). Survey B is composed of a single

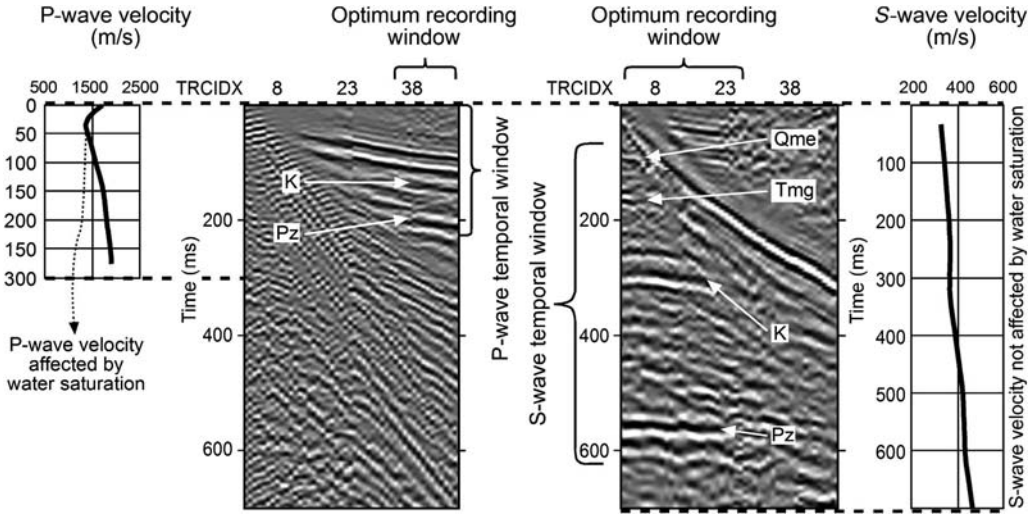

Figure 3. *P*-wave and *SH*-wave walkaway tests are shown on the left and right sides of the figure, respectively. These initial tests were used to define the optimum spatial and temporal recording windows for both energy modes. The *P* wave has a more limited recording window relative to the *SH*-wave data. Also, the *P*-wave stacking velocity curve indicates sensitivity to the groundwater that can often mask the lithologic matrix, whereas the water does not affect the *S*-wave velocity curve.

east–west-oriented *P*-wave line, B1 (40 Hz geophones and 3 m interval). Lines A1, A2-*S*, and A2-*P* were coincidentally acquired, but the two A2 lines were limited to the target fault area (Fig. 2). Lines A1 and A2-*P* provide a resolution comparison between near-surface *SH*- and *P*-wave fault images, respectively (Figs. 3 and 4), and A2-*S* is the multicomponent data acquired in the deformation zone for the *S*-wave splitting analysis. Line A2-*P* is also shown for comparison with line B in order to better visualize the structural correlation (Fig. 4). All common-midpoint data were processed using commercial signal-processing software and followed a standard processing procedure that included coherent noise muting, digital filtering, trace editing, appropriate trace balancing, iterative velocity analyses, surface consistent statics, and poststack Kirchhoff depth migration. All data were acquired with a 24-bit, 48-channel engineering seismograph. *SH*-wave energy was generated by three to five horizontal impacts of a 0.9 kg hammer on a 3 kg modified H-pile section oriented perpendicular (and radial for line A2-*S*) to the spread. The pile flanges were placed in prepared slit trenches to improve the energy couple. To ensure the accurate identification of *S*-wave energy, double-sided impacts and polarity reversals were recorded. The *P*-wave energy was generated by a vertical strike of a 4 kg hammer on a 225 cm^2 hardened aluminum plate.

The approximately 790 m long line A-1 is the highest-quality image from the entire dataset; four prominent coherent and continuous reflectors (Pz, K, Tmg, and Qme) were identified on the section (Figs. 3 and 4). The Pz is the most prominent reflector; it has an average depth of approximately 100 m. The tops of the K and Tmg are also consistent and coherent across with an average 44 m and 24 m depth, respectively. The boundary separating the Qme and overlying loess is the shallowest reflection event (~10 m) resolved in the entire dataset, thus providing the best temporal constraint. Four prominent structural observations can be interpreted on A1; however, the fault of interest is bounded between trace numbers 125 and 225 with an apparent southwest downthrow. The total displacement Pz reflector is nearly 25 m. The fault displacement extends above the Pz and disturbing the K, Tmg, and Qme but with smaller offsets on younger sediment. The 200 m long line A2-*P* also images the fault at the same stationing but with less detail (i.e., only the Pz and K horizons are clearly resolved) (Fig. 4). Line B is approximately 760 m long and is oriented orthogonal to survey A (Figs. 2 and 4). The Pz is the most prominent event in the section at ~107 m depth. The K is a weak event at approximately 45 m depth, near the uppermost limit of the section. The lower fold and larger near-offset (i.e., reduction in optimal temporal recording window) associated with line B are primarily responsible for the lack of K resolution and coherency. This may also have resulted in poorer velocity control, thus explaining the small elevation difference in the Pz event. The fault interpreted between stations 325 and 375 displays just over 20 m of east downthrow and has a similar deformation style and appearance as that exhibited by the line A2-*P* fault. The interpreted faults in lines B and A2-*P* are correlated with a resultant N61°E strike.

Birefringence: Data Acquisition, Rotation, and Complexities

Multicomponent geophones were not available for the *S*-wave splitting acquisition along line A2-*S*; therefore, our four-component data were generated using 24 orthogonal pairs of horizontal single-component geophones and two orthogonal energy source orientations per receiver and shot station, respectively (Fig. 5). Specifically, the data were

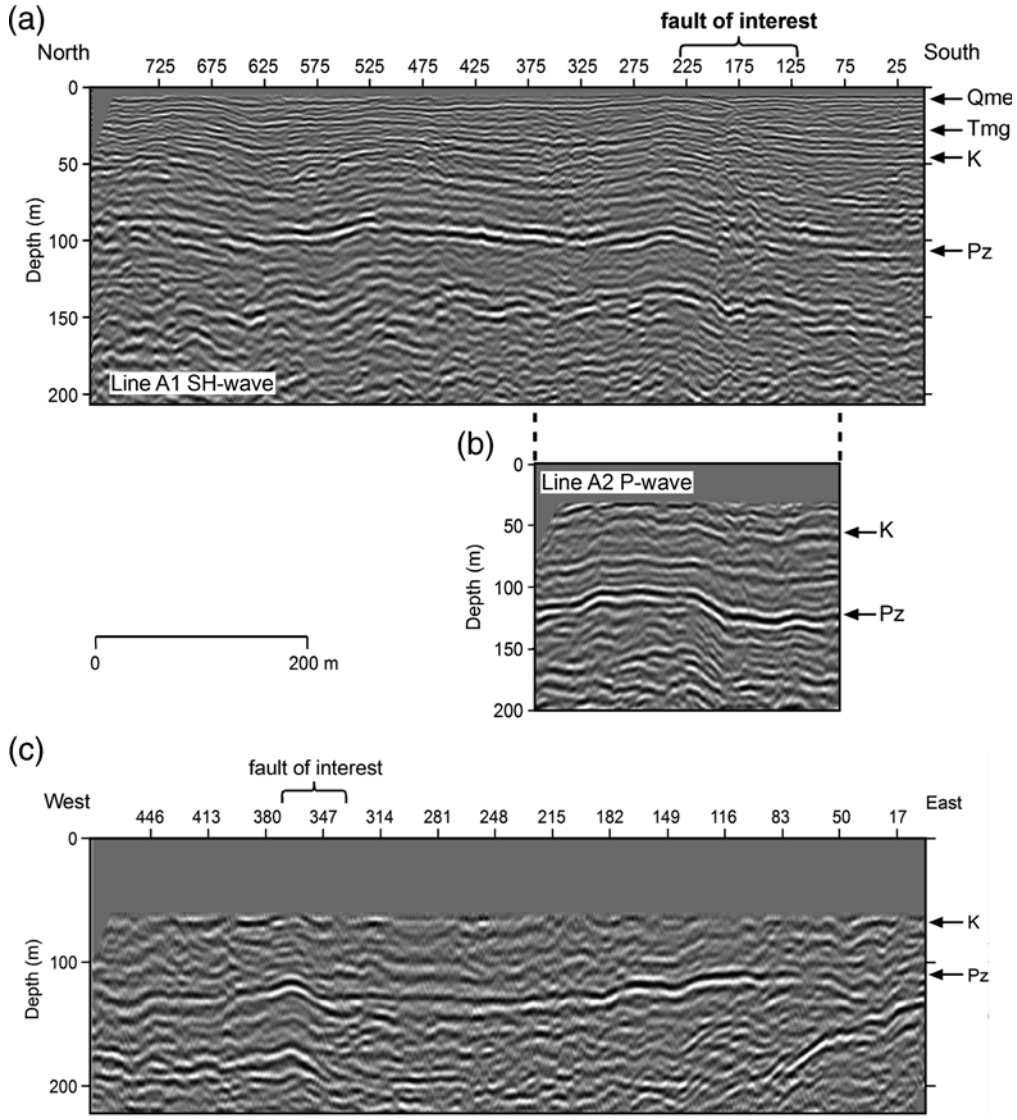

Figure 4. (a) Line A1 and (b) line A2-*P* are stacked depth-migrated images. Lines A1 and A2-*P* are also coincidently collected *SH*- and *P*-wave reflection profiles, respectively. (c) Stacked depth-migrated line B image.

collected along an N20°E-oriented highway with an initial transverse-source–transverse-receiver (TT) and transverse-source–radial-receiver (TR) at each receiver and shot station. Prior to rolling to the next station, the source was rotated 90° to simultaneously record the radial-source–transverse-geophone (RT) and radial-source–radial-geophone (RR) data. This procedure was similar to Harris (1996) except additional recording channels allowed our data to be collected in one rather than two passes. In addition, any source direction had six total hammer impacts applied at each shot location, three strikes per side. Each strike was saved individually in order to check and correct for inadvertent time delays (trigger) prior to summing the three strikes per side into a single vertical stack. An identical procedure with the addition of a polarity reversal was performed on the opposing side before all data were stacked into a single record. The stacking process was performed to enhance the signal to noise ratio. This process was repeated separately for both the transverse and radial energy sources. Regardless of transverse or radial source, the transverse-oriented geophones were separated from radial-oriented geophones, creating two datasets for each source orientation. As the transverse-oriented geophones were assigned an odd channel number (1–47) and radial-oriented geophones were assigned an even channel number (2–48) in the field operation, data headers for each grouping were reindexed to assign channel numbers from 1 to 24 for each dataset, TT, TR, RT, and RR. This was a necessary step for efficiently setting the field geometry and calculating velocities in the software's processing domain.

Prior to rotation and interpretation, complexities associated with the arriving signal were characterized (Fig. 6). Specifically, phase, amplitude, and mode changes that generate precursory and subsequent phases beyond the critical angle (Crampin, 1985; Harris, 1996) arise from the free-surface

Figure 5. Photos showing (a) line A2-*S* shear-wave splitting survey along the edge and parallel to the N20°E-oriented county highway. (b) Two orthogonal single-component horizontally polarized 30 Hz geophones and their cable takeout connections. (c) Transverse *SH*-wave source in-line and orthogonal with transverse and radial geophones, respectively. (d) Radial *SH*-wave source in-line and orthogonal with the radial and transverse geophones, respectively.

effect and can manifest in the recorded waveform; therefore, near-surface shear-wave splitting measurements using rotated reflection data become problematic to interpret (i.e., erroneous time-shift artifacts not associated with *S*-wave polarization) without a defined spatial recording threshold or window to suppress this occurrence. The window at which distortion in signal characteristics does not exist (or is minimal) is called the shear-wave window (i.e., incident signals have near-vertical propagation paths to target depths) and is defined by arriving signal with incident angles less than critical (i.e., $\sin^{-1}[V_P/V_S]^{-1}$) through the uppermost low-velocity layer (Booth and Crampin, 1985; Crampin, 1985; Harris, 1996). The refracted data showed an average 10 m thick near-surface layer (i.e., loess) with *P*- and *S*-wave velocity ranges between 468 and 620 m/s, and 213 and 234 m/s, respectively; therefore, the resultant V_P/V_S ratio ranged between 2 and 2.9, defining a maximum shear-wave window boundary from 20° to 30° (Fig. 6). In order to record signal within this window, the line A2-*S* survey used only the first 12 data traces and carefully applied surgical mutes, particularly for the Qme and Tmg events. Although the narrowed window halved the maximum available fold, it precluded the potential for *S*-wave polarization contamination with inadvertent time shifts associated long-offset signal distortion.

All data were processed following the standard procedures, but before the velocity analysis step was performed on the *S*-wave splitting data, a matrix rotation was used to determine the fast (S1) and slow (S2) shear-wave directions (i.e., natural coordinate system) following the procedures described by Alford (1986) and Harris (1996). Specifically, they determined the natural coordinate system by maximizing and minimizing the reflection signal's polarized energy on the main-diagonal and cross-diagonal elements of the data matrix. The natural coordinate system aligns maximum energy (or S1 direction) and minimum energy (or S2 direction) parallel and orthogonal to the inclusion direction, respectively. Consequently, each component (i.e., TT, TR, RT, and RR) was rotated separately at a 5° increment, between

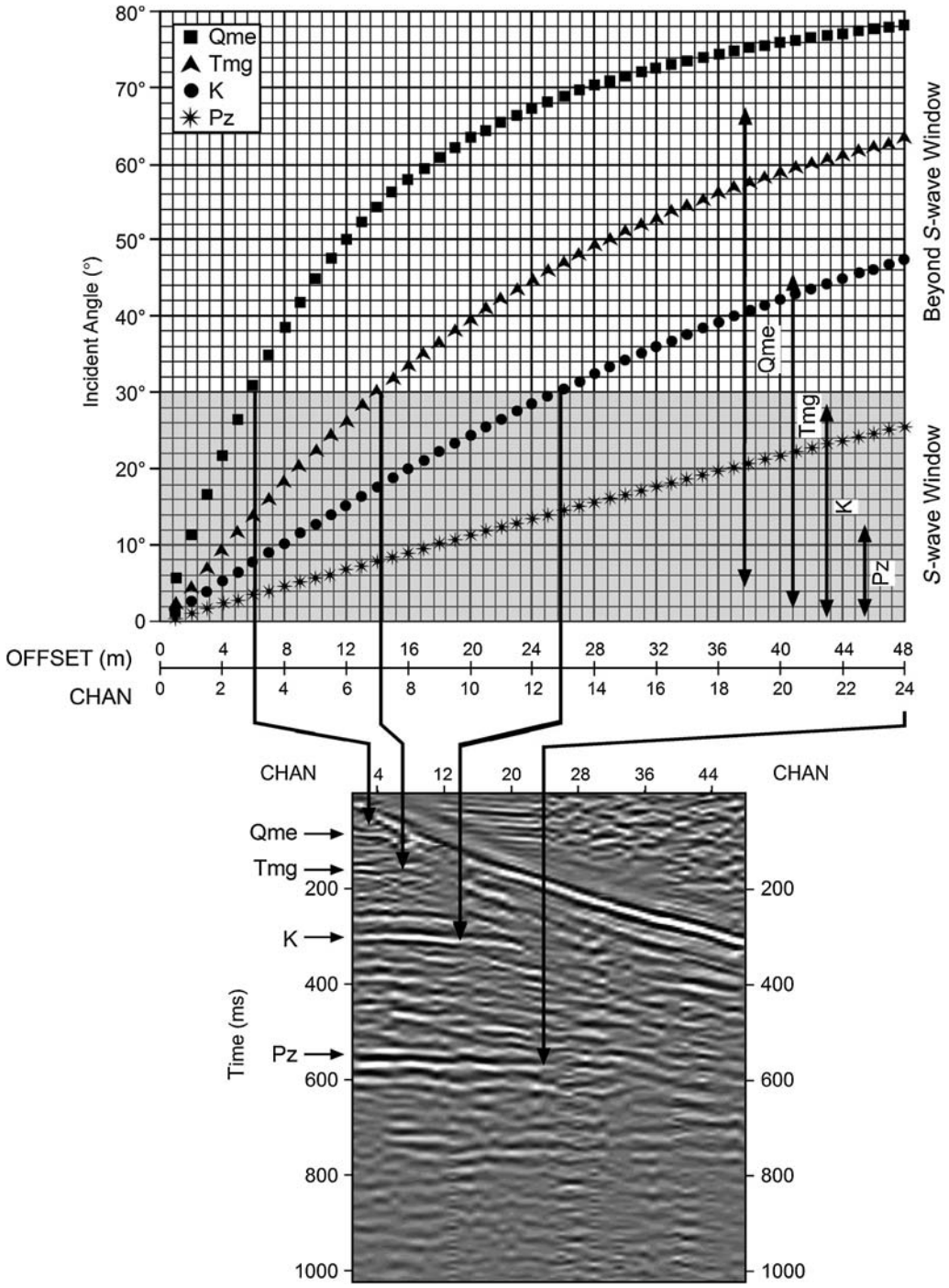

Figure 6. Theoretical schematics and observed shear-wave window on a recorded seismogram are shown in the upper and lower parts of the figure, respectively. Data to the left of the vertical arrows on the seismogram are inside the window; therefore, minimal changes or disturbances in the wavelet characteristics are anticipated. Signals recorded to the right of the arrows on the seismogram are recorded outside the window in which amplitude and phase changes can occur. Therefore, the shear-wave window is where distortion in signal characteristics is minimal and incident signals have near-vertical propagation paths to target depths. Using the criteria described by Booth and Crampin (1985) and Harris (1996), a maximum shear-wave window boundary for these data can be defined between 20° and 30°.

0° and 180° clockwise, and amplitude spectra calculated for each rotation dataset. Figure 7a shows example rotated amplitude spectra at 40° and 130° for the cross-diagonal and main-diagonal components, respectively. Also shown on these plots are the initial unrotated (0° rotation) spectra. The amplitude spectra were normalized using the unrotated amplitude spectrum (Fig. 7b). The difference between the normalized spectral ratios of the cross-diagonal and main-diagonal elements for that particular rotation angle is also shown in Figure 7b. The spectral ratio difference for each

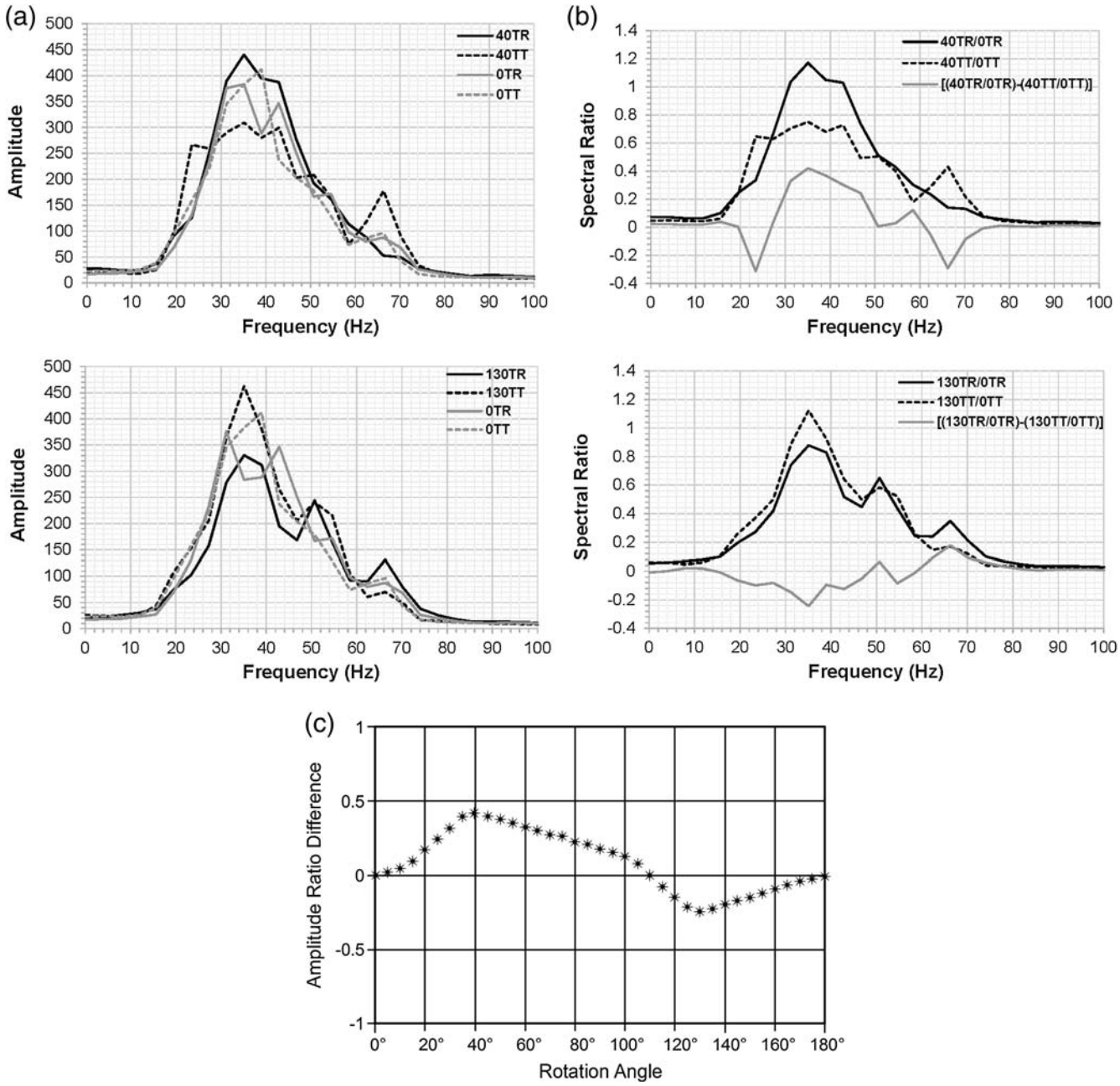

Figure 7. (a) Plot of example amplitude spectra for main-diagonal and cross-diagonal elements rotated at 40° and 130°. The amplitude spectra also show the unrotated (0°) elements. (b) Normalized amplitude spectral ratios were calculated for each element rotation using the unrotated amplitude spectrum. Examples are shown for 40° and 130° rotations along with the difference between the normalized spectral ratios of the cross-diagonal and main-diagonal elements for these particular rotation angles. (c) Spectral ratio difference for each rotation. Because data were collected along the N20°E-oriented highway, the geographic bearings of the fast and slow directions are defined as N60°E and N30°W, respectively.

rotation is plotted in Figure 7c. The results show a maximum amplitude ratio difference between these components at 40° clockwise rotation and the minimum at 130° clockwise rotation. By definition, the 40° rotation represents the fast direction (maximum energy) and 130°, which is orthogonal to the 40° rotation, represents the slow direction (minimum energy). Because line A2-*S* is parallel with the N20°E-oriented highway, the geographic bearings of the fast and slow directions are defined as N60°E and N30°W, respectively. This correlates well with the measured N61°E strike from the two orthogonal seismic profiles. Postrotation processing steps included velocity analysis (normal moveout correction), noise attenuation, sorting, and stacking. A schematic of the element rotations relative to the anisotropic geologic fabric is shown in Figure 8a. A prestack comparison of an S1 and S2 rotated field file and their resultant two-way

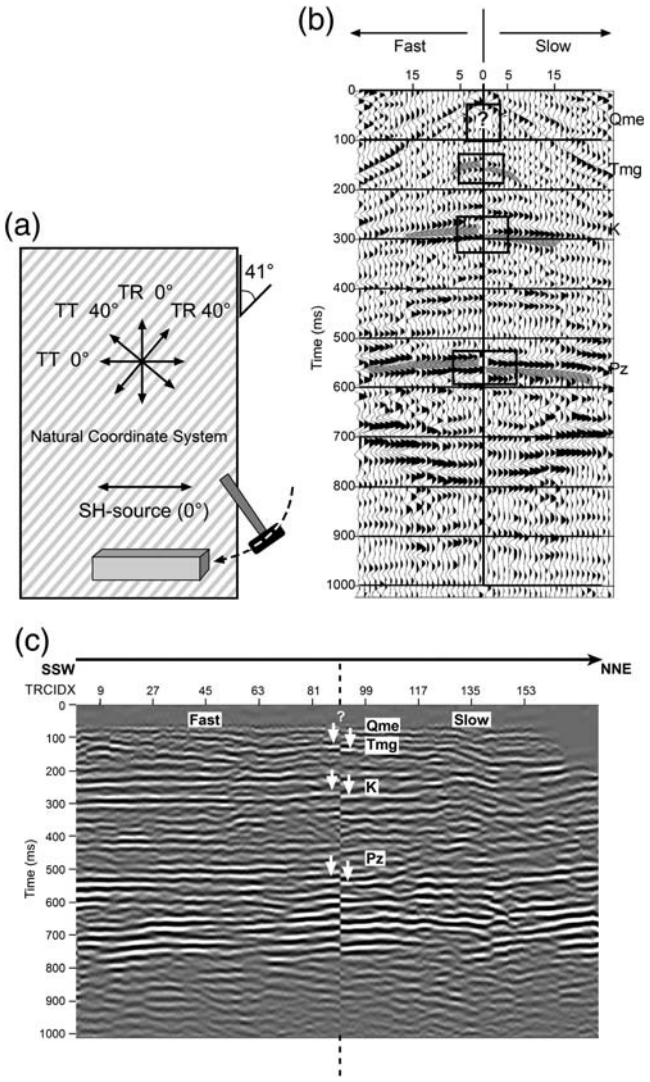

Figure 8. (a) Schematic of the element rotations relative to the well-constrained anisotropic geologic fabric. (b) Example field file shown in a symmetric mirror-view format of the data rotated into the fast S1 and slow S2 components. (c) Stacked A1 image between start point and southwest edge of the fault. The first and second halves of the profile are processed in the S1 and S2 rotations, respectively. The arrows at the seam show the dynamic mistie that result in an azimuthal anisotropy ranging between 2.9% and 4.4%. The magnitude of mistie increased with depth. The mistie was not measured inside the fault zone because of reflector incoherency and difficulty discriminating anisotropic and structural offsets.

travel-time shifts is shown in Figure 8b. The S1 and S2 rotated field file has been spliced in a mirror-image format in order to better exhibit the reflection two-way travel-time shifts. The exhibited time shift, called dynamic mistie, provides a relative measure of the azimuthal anisotropy (Martin and Davis, 1987) and is also manifested in the final stack (Fig. 8c). The stacked image of the fault area has the first and second halves of the profile processed in the S1 and S2 rotations, respectively. The seam was placed in the footwall and just outside the main area of fault deformation where coherent reflection events are still visible for comparison but remain exposed to the fault's zone of influence. The results are typical of shear-wave splitting images found in deeper industry-scale data. Moreover, the arrows at the seam indicate between 9.5 and 15 ms of dynamic mistie in the shallow and deeper reflectors, respectively. This results in an azimuthal anisotropy range between 2.9% (Qme reflection) and 4.4% (Pz reflection), or an average of approximately 3.6% which falls within the reasonable value range (i.e., between 0.5% and 5%) reported by Crampin and Lovell (1991). Although no local anisotropy measurements are available in undisturbed sediment for comparison, we reason that the significant deformation (i.e., microfractures) associated with the faulted sediment is the dominant inclusion and responsible for the measured anisotropy. We note that these results are less equivocal than the Harris (1996) interpretation where he was unsure if the measured anisotropy resulted from tensional stress produced by local uplift or caused by an unimaged nearby fault. We also note these results are significantly higher than the Harris (1996) 2% anisotropy measurements in sediment with similar dynamic properties. We suspect our higher anisotropy values are a result of the structural proximity with our measurements.

Conclusions

The lack of surface evidence for active faults in the NMSZ and other seismically active areas in the central United States (e.g., Wabash Valley seismic zone, etc.) necessitates the use of shallow geophysics, primarily *P*- and *S*-wave reflection techniques, to identify and characterize the near-surface structure. The results and data interpretations for this study indicate that shear-wave birefringence measurements provide an additional tool for evaluating the azimuthal characteristics of a neotectonic inclusion. This can also be particularly useful for areas with limited access (i.e., urban areas) where widespread data acquisition and surveying is prohibitive. Having said that, acquisition and processing of shear-wave splitting data are much more laborious and time intensive than traditional seismic reflection methods; the use of calibrated three-component exploration geophones not available to this study however, would certainly improve the method efficiency and quality of results. In addition, we believe that integrating downhole shear-wave splitting methods with the surface methods would significantly enhance anisotropic resolution in general, but specifically for complex areas that are exposed to a vertically varying azimuthal anisotropy. Nonetheless, taking advantage of shear-wave polarization characteristics in areas lacking geomorphic manifestations for active seismicity can be helpful for determining the geometry and extent of neotectonic deformation in the context uncertainty reduction for seismic-hazard calculations.

Data and Resources

All data presented in this study were collected and processed by faculty and students at the University of Kentucky.

Unprocessed or processed versions are available from the authors. The seismic signal processing was performed with VISTA13 by Schlumberger-GEDCO. Topographic and fault information used for Figure 2 were constructed with maps downloaded from the Kentucky Geological Survey using http://kgs.uky.edu/kgsweb/main.asp (last accessed January 2013).

Acknowledgments

This work was financially supported by the Department of Energy/Kentucky Research Consortium for Energy and Environment (Award DE-FG05-03OR23032) and U.S. Geological Survey–National Earthquake Hazards Reduction Program (Award 01HQGR0044). Additional support came from the Kentucky Geological Survey (KGS). The authors wish to thank two anonymous reviewers, as well as Associate Editor Delphine Fitzenz and Editor-in-Chief Diane Doser for their helpful comments that improved the manuscript. We also thank Collie Rulo (KGS) for her graphic arts assistance and Jamie Harris for his helpful data processing suggestions.

References

Alford, R. (1986). Shear data in the presence of azimuthal anisotropy: Dilley, Texas, *56th Ann. Internat. Mtg., Soc. Expl. Geophys. Expanded Abstracts*, 476–479.

Booth, D. C., and S. Crampin (1985). Shear-wave polarizations on a curved wavefront at an isotropic free-surface, *Geophys. J. Roy. Astron. Soc.* **83,** 31–45.

Crampin, S. (1985). Evaluation of anisotropy by shear-wave splitting, *Geophysics* **50,** 142–152.

Crampin, S., and J. H. Lovell (1991). A decade of shear-wave splitting in the Earth's crust: What does it mean? What use can we make of it? And what should we do next? *Geophys. J. Int.* **107,** 387–407.

Harris, J. B. (1996). Shear-wave splitting in Quaternary sediments: Neotectonic implications in the central New Madrid Seismic Zone, *Geophysics* **61,** 1871–1882.

Kolata, D. R., and W. J. Nelson (1991). Tectonic history of the Illinois basin. In interior cratonic basins, special issue, *Am. Assoc. Petrol. Geol. Memoir* **51,** 263–292.

Long, M. D., and P. G. Silver (2009). Shear wave splitting and mantle anisotropy: Measurements, interpretations, and new direction, *Surv. Geophys.* **30,** 407–461.

Martin, M. A., and T. L. Davis (1987). Shear-wave birefringence: A new tool for evaluating fractured reservoirs, *The Leading Edge* **6,** 22–28.

Nelson, W. J., F. B. Denny, L. R. Follmer, and J. M. Masters (1997). Tertiary and Quaternary tectonic faulting in southernmost Illinois, *Eng. Geol.* **46,** 235–258.

Nelson, W. J., F. B. Denny, L. R. Follmer, and J. M. Masters (1999). Quaternary grabens in southernmost Illinois: Deformation near an active intraplate seismic zone, *Tectonophysics* **305,** 381–397.

Olive, W. W. (1980). Geologic maps of Jackson Purchase Region, Kentucky. *U.S. Geol. Surv. Map I-1217*, 1 sheet, 11 pp.

Schoenberg, M., and M. Sayers (1995). Seismic anisotropy of fractured rock, *Geophysics* **60,** 204–211.

Sexton, J. L. (2006). Lithologic and stratigraphic compilation of near-surface sediments for the Paducah Gaseous Diffusion Plant, McCracken County, KY, *Master's Thesis*, submitted to the Graduate School at University of Kentucky, 250 pp.

Verdon, J. P., and J. M. Kendall (2011). Detection of multiple fracture sets using observation of shear-wave splitting in microseismic data, *Geophys. Prospect.* **59,** 593–608.

Wheeler, R. L. (1997). Boundary separating the seismically active Reelfoot rift from the sparsely seismic Rough Creek graben, Kentucky and Illinois, *Seismol. Res. Lett.* **68,** 586–598.

Woolery, E. W., and R. Street (2002). Quaternary fault reactivation in the Fluorspar Area Fault Complex of western Kentucky: Evidence from shallow *SH*-wave reflection profiles, *Seismol. Res. Lett.* **73,** 628–639.

Woolery, E., J. Baldwin, K. Kelson, S. Hampson, R. Givler, and S. Sundermann (2009). Site-specific fault hazard assessment—Fluorspar Area Fault Complex, western Kentucky, *Seismol. Res. Lett.* **80,** 1035–1044.

University of Kentucky
Department of Earth and Environmental Sciences
101 Slone Research Building
Lexington, Kentucky 40506-0053
woolery@uky.edu
(E.W.W.)

University of Basra
Department of Geology
1846 Garmat Ali Street
Basra, Iraq
azal222@g.uky.edu
(A.A.)

Manuscript received 6 June 2013;
Published Online 27 May 2014